Opto-Electronic Advances

CN 51-1781/TN ISSN (Print) 2096-4579 ISSN (Online) 2097-3993

Ultra-sensitive multi-band infrared polarization photodetector based on 1T'-$MoTe_2$/2H-$MoTe_2$ van der Waals heterostructure

Yuting Pan, Lidan Lu*, Bofei Zhu, Chunhua An, Jing Yu, Guanghui Ren, Jian Zhen Ou*, Mingli Dong*, Zheng You* and Lianqing Zhu*

Citation: Pan YT, Lu LD, Zhu BF, An CH, YU J, REN GH, OU JZ, DONG ML, YOU Z, ZHU LQ. Ultra-sensitive multi-band infrared polarization photodetector based on 1T'-$MoTe_2$/2H-$MoTe_2$ van der Waals heterostructure. *Opto-Electron Adv* **9**, 250260 (2026).

https://doi.org/10.29026/oea.2026.250260

Received: 26 September 2025; Accepted: 16 December 2025; Published online: 9 February 2026

Opto-Electronic Advances

Article

March 2026, Vol. 9, No. 3

Open Access

Ultra-sensitive multi-band infrared polarization photodetector based on 1T'-$MoTe_2$/2H-$MoTe_2$ van der Waals heterostructure

Yuting Pan[1,3], Lidan Lu[1]*, Bofei Zhu[2], Chunhua An[4], Jing Yu[1], Guanghui Ren[5], Jian Zhen Ou[5]*, Mingli Dong[1]*, Zheng You[2]* and Lianqing Zhu[1]*

Abstract: Near infrared polarized photodetectors are widely used, and van der Waals heterostructures based on transition metal dichalcogenides are important platforms for device research and application. Homologous polymorphic two-dimensional chalcogenides refer to two-dimensional chalcogenides with the same chemical composition but different crystal structures. Homologous polymorphic two-dimensional chalcogenides have shown great potential in near-infrared detection due to their unique bandgap characteristics, exciton effects, and controllable optoelectronic properties. This paper studies a near-infrared polarized photodetector based on 1T'-$MoTe_2$/2H-$MoTe_2$ structure, in which the semimetallic 1T'-$MoTe_2$ has attracted attention due to its low work function and excellent electrical performance. 1T'-$MoTe_2$ and 2H-$MoTe_2$ form a favorable bandgap structure after forming a heterojunction, which improves carrier separation efficiency and photoelectric response. This device exhibits excellent high-sensitivity optoelectronic detection performance in the wideband region (532–2200 nm), such as significant high responsivity (3.06 $A \cdot W^{-1}$) under 1310 nm laser, specific detectivity (3.2×10^9 Jones), good external quantum efficiency (289%), and fast rise and decay response times of 10.56 ms/6.26 ms. In addition, the device has polarization detection capability, achieving a high polarization sensitivity of 20.1. The device has successfully achieved imaging from visible light to near-infrared light, highlighting the potential of 1T'-$MoTe_2$/2H-$MoTe_2$ heterojunction as a polarization sensitive detector.

Keywords: heterojunction; $MoTe_2$; polarization; shortwave

DOI: 10.29026/oea.2026.250260 | CSTR: 32247.14.oea.2026.250260

Citation: Pan YT, Lu LD, Zhu BF et al. Ultra-sensitive multi-band infrared polarization photodetector based on 1T'-$MoTe_2$/2H-$MoTe_2$ van der Waals heterostructure. *Opto-Electron Adv* **9**, 250260 (2026).

1 Introduction

The development of polarized light detection technology has facilitated people's production and life. In addition to extracting amplitude and frequency information of light, it can also extract polarization information of light to provide more and clearer information about imaging objects (such as surface roughness, texture shape, etc.). It has important applications in medical diagnosis[1], fiber optic communication[2], aerospace and other fields[3]. The existing polarization sensitive photodetectors usually add additional components such as lenses or gratings on the detector, which not only increases the cost but also increases the complexity of the system, which is not conducive to the development of product commercialization[4]. Therefore, there is an urgent need to develop miniaturized, highly integrated, and structurally simple polarization photodetectors.

Due to different detection mechanisms, photodetectors can be further classified into different types, including photoconductive detectors (PbSe[5], PbS[6], InSb[7]), photovoltaic detectors (Si[8], Ge[9], HgCdTe[10], InAs[11], InSb[12]), and quantum well detectors (GaAs/AlGaAs[13], InGaAs/InP[14]).

Received: 26 September 2025

Accepted: 16 December 2025

Published online: 9 February 2026

[1]School of Instrument Science and Opto-Electronics Engineering, Beijing Information Science and Technology University, Beijing 100192, China; [2]Department of Precision Instruments, Tsinghua University, Beijing 100084, China; [3]School of Opto-electronic Engineering, Changchun University of Science and Technology, Changchun 130022, China; [4]School of Precision Instruments and Optoelectronic Engineering, Tianjin University, Tianjin 300072, China; [5]School of Engineering, RMIT University, Melbourne 3000, Australia.

*Correspondence: LD Lu, E-mail, lldan_dido@bistu.edu.cn; JZ Ou, E-mail: jianzhen.ou@rmit.edu.au; ML Dong, E-mail: dongml@bistu.edu.cn; Z You, E-mail: yz-dpi@mail.tsinghua.edu.cn; LQ Zhu, E-mail: zhulianqing@bistu.edu.cn

However, most traditional photodetectors can only detect specific wavelength ranges, have high dark currents, require consideration of lattice matching issues, and also require complex growth processes, increased external energy sources, complex cooling systems, and other issues. All of these have increased the complexity and cost of the system. In recent years, with the rapid development of two-dimensional materials, many people have studied devices that achieve different functions by constructing heterojunctions of different materials and overcoming the limitations of lattice matching[15]. Materials with in-plane anisotropic crystal structures have been explored as potential polarization sensitive photodetectors, which can utilize the asymmetry of material structures to directly identify the polarization information of incident light without the need for additional components. For example, materials with anisotropic structures such as GeSe[16], $GeSe_2$[17], ReS_2[18], $ReSe_2$[19], SnS[20], InSe[21], and black phosphorus (BP)[22] have been explored in polarized photodetectors. GeSe, ReS_2, and $ReSe_2$ have large band gaps and are difficult to respond to near-infrared wavelengths, while materials such as BP, InSe, and GeSe are unstable in air and their device performance is prone to degradation. A single GeSe polarization detector has an optimal polarization ratio of 2.16 at 808 nm, but faces the problem of low polarization sensitivity[23].

Homologous polymorphic two-dimensional chalcogenides refer to two-dimensional chalcogenides with the same chemical composition but different crystal structures. TMDCs of different crystal phases (such as 1T' phase and 2H phase) exhibit significant differences in electrical, optical and mechanical properties, which provides the possibility for diversified applications of the materials. $MoTe_2$ is a polymorphic material consisting of a semiconductor 2H phase and a metastable semimetal 1T'-phase[24]. The single-layer 2H phase is a honeycomb structure, while the 1T'-phase is a twisted central honeycomb structure. 1T'-$MoTe_2$, as a new type of two-dimensional topological semimetal, has a gapless electronic structure and excellent optoelectronic properties, which make it show great potential in the field of infrared detection. Its unique crystal structure also gives it the ability to detect polarized light.

Therefore, this article proposes a photodetector with a 1T'-$MoTe_2$/2H-$MoTe_2$ structure, which provides a promising platform for polarization sensitive photodetectors. The 2H-$MoTe_2$ and 1T'-$MoTe_2$ are stacked layer by layer to form a van der Waals heterojunction. The previous research on this junction did not analyze its near-infrared detection performance[25], so the focus of this study is to explore the performance of 1T'-$MoTe_2$/2H-$MoTe_2$ hetero-structure as a near-infrared photodetector, especially for detecting polarized light. The results show that the photodetector has good comprehensive detection performance, capable of detecting light in the 532–2200 nm wavelength range. It has high responsivity rate of 3.06 $A \cdot W^{-1}$ at 1310 nm, high detection rate of 3.2×10^9 Jones, high EQE of 289%, and rapid rise and fall response times of 10.56 ms/6.26 ms. The 1T'-$MoTe_2$/2H-$MoTe_2$ hetero-structure exhibits low dark current and high photo-responsiveness in self driven photo-detection.

2 Experimental section

2.1 Device manufacturing

The 1T'-$MoTe_2$/2H-$MoTe_2$ heterojunction device was fabricated using a standard dry transfer process. Initially, thin flakes of 1T'-$MoTe_2$ and 2H-$MoTe_2$ were obtained from their bulk crystals via mechanical exfoliation using blue tape and subsequently transferred onto polydimethylsiloxane stamps mounted on glass slides. Under optical microscope observation and alignment assistance, the exfoliated flakes were precisely stacked layer-by-layer onto a p-type silicon substrate with a 285 nm SiO_2 layer using a precision transfer system, thereby constructing the heterostructure.

After heterojunction formation, a layer of 950 PMMA A6 e-beam resist was spin-coated onto the structure serving as both a protective layer and patterning medium. Electrode patterns were then defined using electron beam lithography. Subsequently, a 5 nm thick chromium adhesion layer and a 60 nm thick gold layer were deposited as metal electrodes via electron beam evaporation. The final electrode structure was achieved through a lift-off process to remove residual PMMA and excess metal. Finally, the device was annealed at 200 °C for 3 minutes in a nitrogen atmosphere to effectively remove residual organic contaminants and moisture at the interfaces while significantly improving the contact characteristics between the metal electrodes and the two-dimensional materials.

2.2 Electrical and optoelectronic measurements

Observing the morphology and structure of heterojunction devices using an optical microscope, characterizing the morphology and thickness of the devices using a Park atomic force microscope, and measuring the Raman spectra of the materials using a Raman spectrometer under 532 nm laser. All electrical measurements of the 1T'-$MoTe_2$/2H-$MoTe_2$ heterostructure device were taken using a low-temperature probe stage (CRX-VF) and a semiconductor analyser (Keysight B1500A), with the light source being a single point laser of different wavelengths with a uniform diameter of approximately 1 mm.

3 Results and discussion

3.1 Manufacturing and characterization of 1T'-$MoTe_2$/2H-$MoTe_2$ heterojunction

Figure 1(a) is a three-dimensional (3D) schematic diagram of the proposed 1T'-$MoTe_2$/2H-$MoTe_2$ (Shenzhen Six Carbon Technology Co., Ltd.) photodetector, with 2H-$MoTe_2$ at the bottom and 1T'-$MoTe_2$ at the top. The two materials are vertically stacked to form a heterostructure, and the metal electrode Cr/Au (5 nm/60 nm) is deposited on both materials. The detailed manufacturing process of this heterostructure device can be found in the experimental section. The optical microscope image of the device is shown in Fig. 1(b), and the atomic force microscope (AFM) image of the 1T'-$MoTe_2$/2H-$MoTe_2$ heterojunction is shown in Fig. S1(a), where the inset shows the thickness of the two materials. According to the AFM test results, the thickness of 2H-$MoTe_2$ and 1T'-$MoTe_2$ is 31 nm and 32 nm, respectively. The Raman spectra of each material are shown in Fig. S1(b). For a single $MoTe_2$, the main Raman peaks appear at 173 cm^{-1} and 234 cm^{-1}, corresponding to the A_{1g} and E_{2g} modes, respectively[26]. The typical Raman modes of 1T'-$MoTe_2$ include A_g (75, 125, 160, 257 cm^{-1}) and B_g (108 cm^{-1}) modes[27]. The Raman spectra of their heterojunction regions contain characteristic peaks of 2H-$MoTe_2$ and 1T'-$MoTe_2$, indicating interlayer coupling between the two materials. However, the 2H-$MoTe_2$ peak is relatively small, and the top 1T'-$MoTe_2$ layer suppresses the excitation laser from penetrating 2H-$MoTe_2$. Figure S1(c) shows the spatial photocurrent mapping of the heterojunction, where significant photocurrent is generated in the junction region under 532 nm laser irradiation. Figure S1(d) shows the transfer characteristic of 2H-$MoTe_2$, with drain voltage (V_{ds}) fixed at 1 V. Indicating that 2H-$MoTe_2$ is a p-type semiconductor material. Figure S1(e–f) show the output characteristic of 2H-$MoTe_2$ and 1T'- $MoTe_2$. From the output curve (I_{ds}-V_{ds}) of the 2H $MoTe_2$ transistor, significant nonlinear characteristics can be observed, indicating that a Schottky contact is formed between the metal electrode and the 2H $MoTe_2$ channel, rather than an ideal ohmic contact. And the curve in Fig. S1(f) indicates the semi metallic properties of 1T'-$MoTe_2$. The KPFM measurement of 2H-$MoTe_2$/1T'-$MoTe_2$ is shown in Fig. S2(a), and the results indicate that the surface potential of 1T'-$MoTe_2$ is about 330 mV higher than that of 2H $MoTe_2$, revealing that the former has a higher Fermi level and lower work function. Based on these findings, we constructed energy band diagrams of the heterojunction (Fig. 1(c) and 1(d)). The band structure before contact between 2H-$MoTe_2$ and 1T'-$MoTe_2$ is shown in the Fig. 1(c). The bandgap of 2H-$MoTe_2$ is about 1 eV[28], and the work function of 1T'-$MoTe_2$ at 32 nm is about 4.4 eV[29]. There is a significant band shift between 1T'-$MoTe_2$ and 2H-$MoTe_2$. The band structure after contact between 2H-$MoTe_2$ and 1T'-$MoTe_2$ is shown in the Fig. 1(d). Upon contact, Fermi level alignment generates a built-in electric field at the interface, directed from 1T'-$MoTe_2$ toward 2H-$MoTe_2$. Notably, the orientation of this field aligns with the intrinsic built-in electric field at the Au/2H-$MoTe_2$ interface. The superposition of these co-directional electric fields substantially enhances the driving force for photogenerated carrier separation. Crucially, photogenerated carriers are efficiently produced primarily within the depletion region on the 2H-$MoTe_2$ side. Under the synergistic effect of these dual built-in fields, the electron-hole pairs are rapidly separated: electrons are swept toward the 1T'-$MoTe_2$ side, while holes are driven toward the Au electrode.

3.2 Electrical and optical properties of 1T'-$MoTe_2$/2H-$MoTe_2$ device

In order to explore the electrical properties of 1T'-$MoTe_2$/2H-$MoTe_2$ heterojunction, the electrical properties

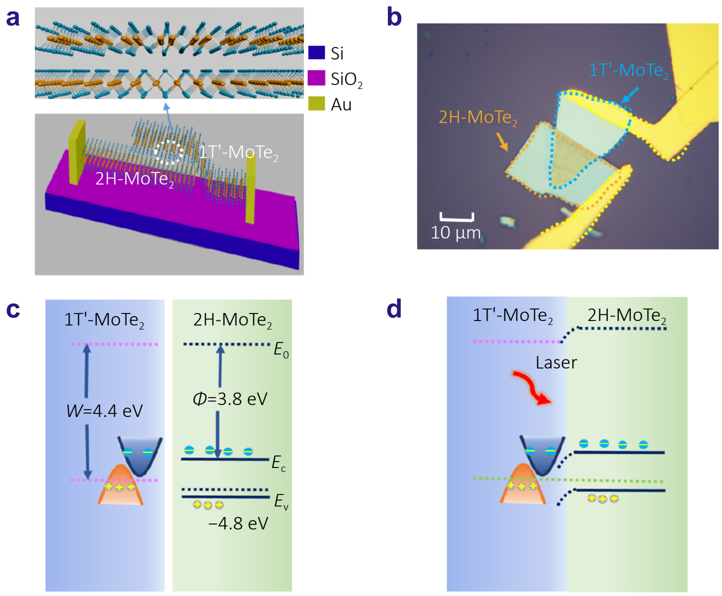

Fig. 1 | (a) Schematic diagram of heterojunction structure of 1T'-$MoTe_2$/2H-$MoTe_2$. (b) Optical image of 1T'-$MoTe_2$/2H-$MoTe_2$ heterojunction prepared. Schematic diagram of the energy band diagrams of 2H-$MoTe_2$ and 1T'-$MoTe_2$ before contact (c) and after contact (d).

of its single materials were tested separately. Figure S1(d–f) shows the transfer and output characteristic curves of 2H-$MoTe_2$ and 1T'-$MoTe_2$, where 2H-$MoTe_2$ is a p-type material and 1T'-$MoTe_2$ is a semi metallic material. Taking the 1310 nm laser light source as an example, the current voltage (I_{ds}-V_{ds}) curve at zero gate voltage is shown in Fig. 2(a). As the optical power density increases, I_{ds} also increases significantly, which is attributed to the increase of photogenerated carriers. At a bias voltage of 1 V, I_{ds} reaches its maximum of 3.298 μA when the optical power density is 806 μW/mm². The *I*-*V* curve measured on a logarithmic scale is shown in Fig. S2(b). The rectification behavior can be more clearly observed from the *I*-*V* curve plotted on the logarithmic scale. Figure 2(b) shows the relationship between open circuit voltage, short-circuit current, and power density. As the optical power density increases, the open circuit voltage and short-circuit current also continue to increase. The functional relationship between the switching ratio (I_{ph}/I_{dark}) and the optical power density under zero bias is extracted in Fig. 2(c). The photocurrent (I_{ph}) is calculated based on the equation $I_{ph}=I_{ds}-I_{dark}$, where I_{dark} is the dark current. The I_{ph}/I_{dark} value increases continuously with the increase of optical power density. When the optical power density is 806 μW/mm², the maximum value is 7×10^4. The figure shows that at multiple power densities, the I_{ph}/I_{dark} value can reach 10^4, indicating that the device has a high switching ratio of up to 10^4 and has great potential for application in photodetectors. Figure S2(c) presents the extracted photocurrent (I_{ph}) as a function of optical power density under a 1 V bias. The relationship between the photogenerated current and optical power density can be well fitted by a power-law equation: $I_{ph} \propto P^{\alpha}$, where I_{ph} and P represent the photocurrent and optical power density, respectively, and α is the fitting parameter indicating linearity. The fitting result yields an α value of 0.77, demonstrating good linearity of the device.

Responsivity (R), specific detectivity (D^*), and external quantum efficiency (EQE) are key factors affecting the performance of photodetectors[30]. Response rate represents how much photocurrent can be generated per unit incident power on the photodetector, calculated as $R=I_{ph}/PS$, where R is the response rate and S is the effective illuminated area. Figure 2(d) shows the response rate of 1T'-$MoTe_2$/2H-$MoTe_2$ heterojunction devices under 1310 nm laser light source irradiation at 1 V and 0 V bias voltages. As the light density increases, the response rate shows a trend of first increasing and then gradually decreasing. At a power density of 679 μW/mm², the response rate is the highest, at 0.02 A/W (0 V bias) and 3.06 A/W (1 V bias), respectively. The formula for calculating the specific detectivity is $D^*=RS^{1/2}/(2qI_{dark})^{1/2}$, where q is the electron charge. The specific detection rate also increases first and then gradually decreases with power density, as shown in Fig. 2(e). At a power density of 679 μW/mm², it is 2.6×10^{11} Jones (bias voltage of 0 V) and 3.2×10^9 Jones (bias voltage of 1 V), respectively. Calculating the specific detectivity through direct measurement of the noise power spectral density is the most accurate method for evaluating detector performance, while the approach based on the shot noise of the dark current may lead to an overestimation of the detectivity.

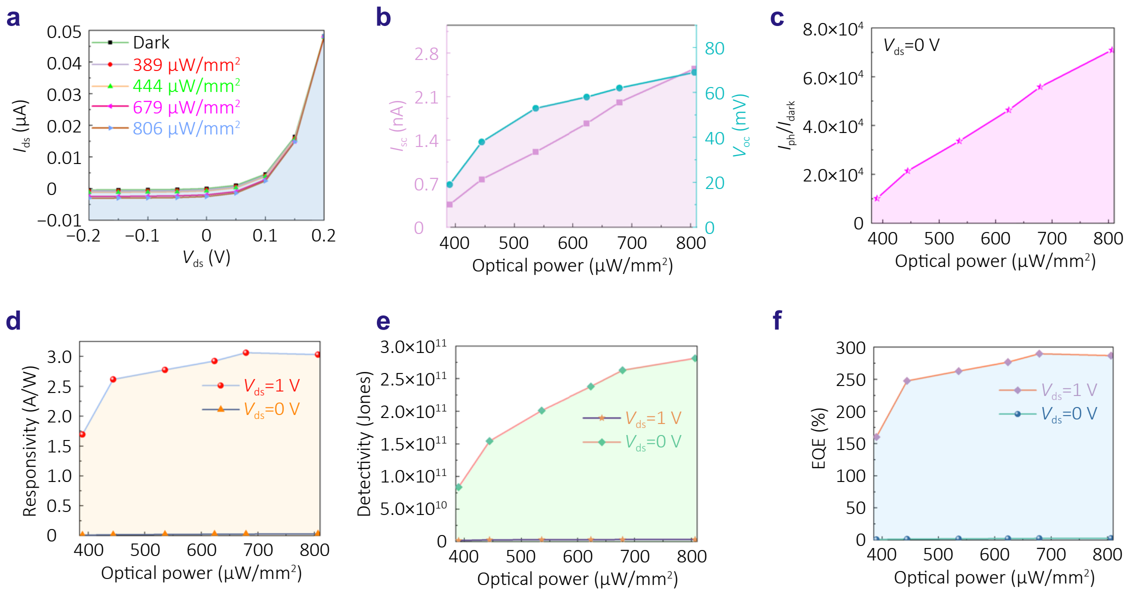

Fig. 2 | (a) The I_{ds}-V_{ds} curves of heterojunction under 1310 nm laser irradiation with different optical power densities and dark conditions. (b) The short-circuit current and open circuit voltage of the device at 1310 nm under different power densities. (c) The curve of switch ratio and optical power density under 1310 nm irradiation at 0 V. The responsivity (d), specific detectivity (e), and external quantum efficiency (f) of heterojunction under 1310 nm laser as a function of optical power density.

EQE is the external quantum efficiency, which is the ratio of the number of excited charge carriers to the number of incident photons. Its calculation formula is $EQE=hcR\lambda^{-1}e^{-1}$, where h is Planck's constant, c is the speed of light, and e is the electron charge. The trend of quantum efficiency changing with light density is the same as the responsivity. At a power density of 679 μW/mm², the *EQE* is 2.54% (bias voltage of 0 V) and 289% (bias voltage of 1 V), respectively. In the 2H-$MoTe_2$/1T'-$MoTe_2$ heterostructure, photogenerated electrons and holes are separated by the internal built-in potentials. These separated opposite charges create a counteracting Coulomb potential that balances the internal built-in potentials, thereby enhancing the transport current through the structure and ultimately resulting in a measured apparent EQE greater than 100%[31]. In addition, the photoelectric response of the device was tested under different laser illumination from visible light to short wave infrared bands, as shown in Fig. S3–S7, including 1550 nm, 976 nm, 650 nm, 532 nm, and 2200 nm. The results showed that the device has excellent ultra wide spectral response capability.

Figure 3(a) shows the temporal light response of the 1T'-$MoTe_2$/2H-$MoTe_2$ device under the irradiation of a 1310 nm laser source with a power density of 389 μW/mm² at V_{ds}=0 V. By controlling the periodic on-off of the light source, it can be observed that photocurrent is also periodically generated and annihilated. Figure 3(b) and 3(c) show the amplification of the regions where the current rises and falls over time. The rise time is defined as the time taken from 10% to 90% of the total photocurrent, and the fall time is defined as the time taken from 90% to 10% of the total photocurrent. These values should be less than 10.56 ms and less than 6.26 ms, respectively. Due to the limitation of the device's time resolution, there are few adjacent time data points, and the rise and fall times may be smaller than the measured values. In 1T'-$MoTe_2$/2H-$MoTe_2$ devices, effective generation, separation, and recombination of electron hole pairs have been achieved. In addition, the photocurrent response of the device under 1310 nm laser with different power densities was tested without any bias voltage, as shown in Fig. 3(d). As the power density increased from 389 μW/mm² to 1343 μW/mm², the photocurrent increased from 0.5 nA to 3.5 nA. Figure 3(e) and 3(f) show the time current response curves of the device under 1 V and −1 V bias voltages for a 1310 nm laser at a power density of 389 μW/mm², respectively. Under the same power density, the photocurrent of the device significantly increased after applying bias voltage, and the photocurrent at 1 V was even larger. In order to explore the stable light response capability of the device, 650 nm laser and 532 nm laser stable switches were vertically irradiated on the device. Without applying bias voltage to the device, hundreds of light switch cycles were carried out, as shown in Fig. S8. The results showed that the device had stable periodic generation and annihilation of photocurrent under hundreds of switch cycles, indicating that the device had stable light switch response. Figure S9 displays the transient photocurrent response of the device under 532 nm laser illumination at driving frequencies of 1, 5, 10, and 100 Hz. The results demonstrate that the device generates clear and stable on/off photoresponse waveforms across all tested frequencies, indicating excellent speed characteristics and response stability. Furthermore, as shown in Fig. S10, the device exhibited

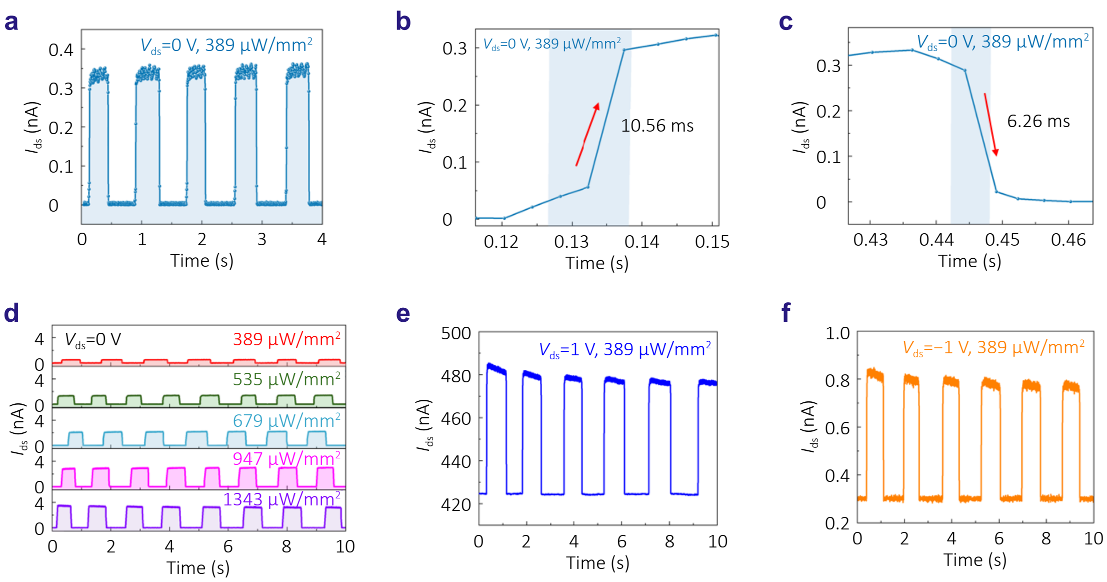

Fig. 3 | (a) The time response of the device under 1310 nm incident light is turned on and off at 0 V bias. (b) The amplification region where the current of a heterojunction increases with time under 1310 nm incident light. (c) The amplification region where the current of a heterojunction decreases over time under 1310 nm incident light. (d) The time response of the device under different power densities of 1310 nm incident light is turned on and off at 0 V bias. The time response of the device under 1310 nm pulsed laser is (e) with a bias voltage of 1 V and (f) with a bias voltage of −1 V.

stable on/off switching characteristics in its transient response under 532 nm pulsed laser illumination at a bias voltage of ±1 V.

3.3 Polarized light detection of 1T'-$MoTe_2$/2H-$MoTe_2$ heterojunction

In order to study the anisotropy of 1T'-$MoTe_2$, angle resolved polarization Raman spectroscopy (ARPRS) was used. The polarizer was rotated at an angle step of 30°, and the polarizer changed from 0° to 360°. The corresponding color images are shown in Fig. 4(a). The results show that the peak intensities at positions such as 108 cm^{-1}, 160 cm^{-1}, and 257 cm^{-1} vary periodically with the polarization angle, with a period of 180°. The peak intensity of Ag mode at 160 cm^{-1} with angle variation was fitted, as shown in Fig. 4(b), and this data can be well fitted using Eq. (1)[32]:

$$I\left(\mathrm{A_g}\right) \propto \left(\cos^2\left(\beta\right) + \frac{a}{b}\cdot\sin^2\left(\beta\right)\cdot\cos\left(\varphi_{ab}\right)\right)^2 + \sin^2\left(\beta\right)\sin^2\left(\varphi_{ab}\right) \ . \quad (1)$$

Among them, β is the angle of linearly polarized light, a and b are the minimum and maximum fitting parameters, respectively, and φ_{ab} is the phase difference between the a and b values in the A_g mode Raman tensor.

To verify the polarization detection capability of the device, a single point laser was converted into linearly polarized light through a polarizer, vertically irradiated onto the device, and the angle of the polarized light was changed by rotating the polarizer in steps of 30°. The schematic diagram of the testing system is shown in Fig. 4(c). The single point laser selected three wavelengths of 650 nm, 976 nm, and 1310 nm for testing, as shown in Fig. 4(d–f), where V_{ds}=0 V. The measured photocurrent data can be well fitted by Eq. (2)[32]:

$$b\left(\beta\right) = b_{\min}\sin^2\left(\beta+\varphi\right) + b_{\max}\cos^2\left(\beta+\varphi\right) \ . \quad (2)$$

In the equation, β is the angle of linearly polarized light, and b_{min} and b_{max} are the minimum and maximum fitting parameters, respectively. The results indicate that the amplitude of the photocurrent of the device varies periodically with the polarization angle at laser wavelengths of 650 nm, 976 nm, and 1310 nm. The light response has strong polarization sensitivity and a period of 180°, which is consistent with the periodicity of the Raman spectrum measured in Fig. 4(a). The anisotropy ratio of photocurrent in the device (defined as the ratio of max (I_{ph}) to min (I_{ph})) is 2.18, 4.75, and 20.1 at 650 nm, 976 nm, and 1310 nm laser wavelengths, respectively, indicating that the device has excellent performance in detecting polarized light. The high anisotropy ratio stems from the intrinsic anisotropic band structure of 1T'-$MoTe_2$ and is significantly enhanced by carrier injection at the device level. The phenomenon of increasing polarization anisotropy ratio with longer wavelengths is primarily attributed to the energy-dependent variation in optical absorption locations within the heterostructure and the intrinsic anisotropy differences among constituent material layers. At shorter wavelengths (e.g., 650 nm), high-energy photons are strongly absorbed by the 2H-$MoTe_2$ layer. With its in-plane isotropic hexagonal crystal structure, 2H-$MoTe_2$ generates photo generated carriers that are separated by the built-in electric field in the junction region, creating a strong polarization-independent isotropic photocurrent background. Although the 1T'-$MoTe_2$ layer simultaneously

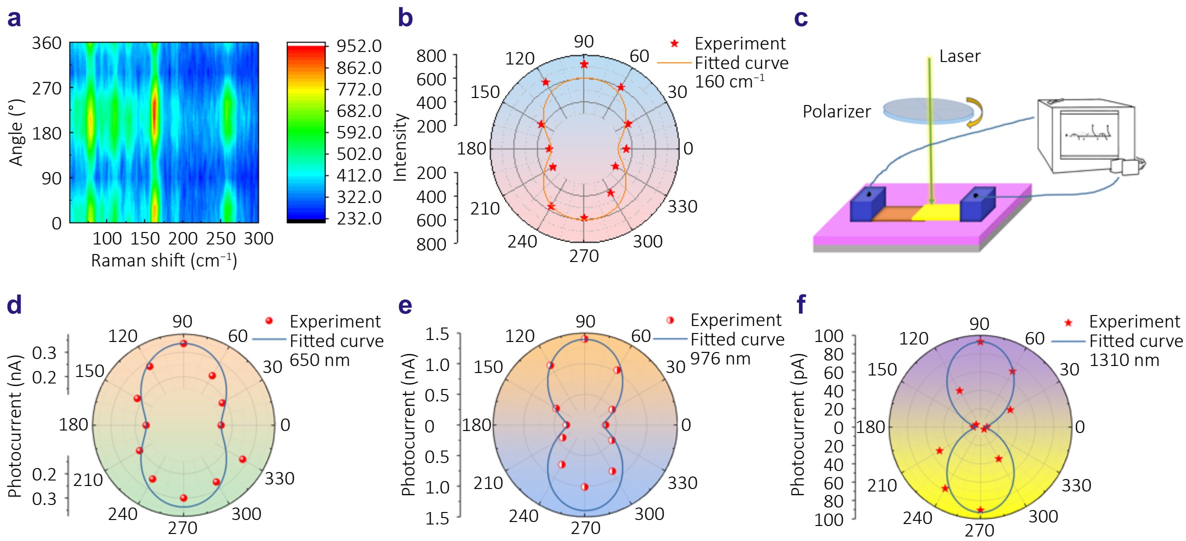

Fig. 4 | (a) The relationship between angle resolved polarization Raman mapping and polarization angle of 1T'-$MoTe_2$ thin films. (b) The polar plot of Raman peak intensity and polarization angle of 1T'-$MoTe_2$ in A_g Raman mode at 160 cm^{-1}, with the orange line as the fitting curve. (c) Schematic diagram of linear polarization sensitive photosensitive detection. When V_{ds}=0 V, the linearly polarized laser wavelengths are (d) 650 nm, (e) 976 nm, and (f) 1310 nm, respectively. And the polarization sensitive photocurrent is a function of the polarization angle in polar coordinates. The blue line represents the fitting curve.

absorbs light and produces anisotropic photocurrent, its contribution becomes "submerged" by this dominant isotropic background from the 2H-$MoTe_2$ layer, resulting in a relatively low overall anisotropy ratio. As the wavelength shifts toward the near-infrared regime, the photon energy gradually drops below the bandgap of 2H-$MoTe_2$, leading to a sharp decline in its absorption coefficient. Consequently, the isotropic photocurrent background becomes significantly attenuated. Meanwhile, the zero-bandgap characteristic of semimetallic 1T'-$MoTe_2$ enables efficient absorption of these longer-wavelength photons. The low-symmetry monoclinic crystal structure of 1T'-$MoTe_2$ confers strong in-plane anisotropy to its optical conductivity. Variations in the angle between incident light polarization and its crystal axes induce substantial modulations in both optical absorption efficiency and resultant photocurrent. At longer wavelengths, this mechanism dominates photocurrent generation, causing the overall device response to be governed entirely by the intrinsic anisotropy of 1T'-$MoTe_2$ and demonstrating significantly enhanced anisotropy ratios.

3.4 1T'-$MoTe_2$/2H-$MoTe_2$ heterojunction polarization imaging

The impressive responsivity and polarization photosensitivity of 1T'-$MoTe_2$/2H-$MoTe_2$ devices have prompted further research on their potential practical applications in broadband and polarization sensitive imaging. Figure 5 shows a schematic diagram of a broadband imaging system, in which a shadow mask plate with a hollow "I" pattern is installed on a 2D mobile platform and located between the heterojunction device and the light source. This allows the mask to move continuously in the *X-Y* direction. When light is blocked by a mask, it cannot reach the device and generate photocurrent. However, when light passes through the hollow pattern of the mask, it illuminates the device, causing the generation of photocurrent, which is then recorded in real time by a semiconductor analyzer. The position resolved photocurrent is transmitted to the computer and converted into a 2D comparison map of photocurrent values, effectively reproducing the patterns present in the mask.

Subsequently, Fig. 6(a–d) show the "I" imaging images

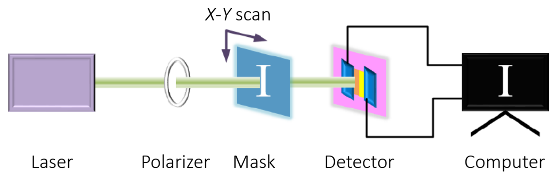

Fig. 5 | System schematic diagram of single point imaging application for 1T'-$MoTe_2$/2H-$MoTe_2$ device.

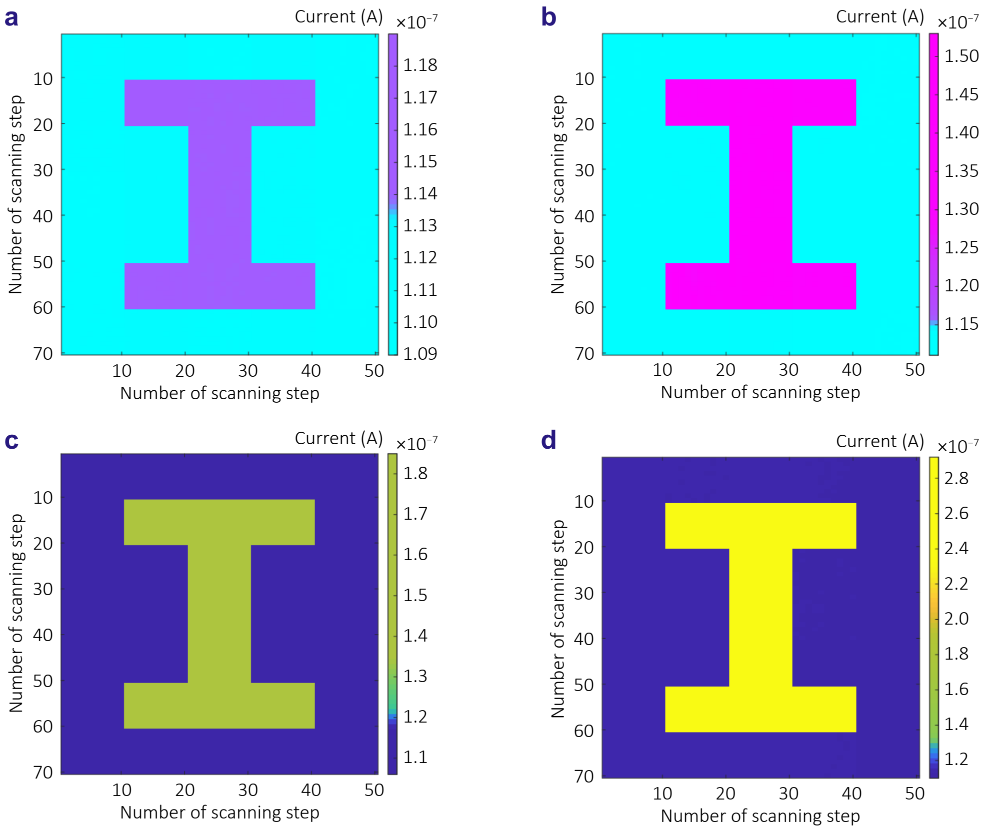

Fig. 6 | (a, b) is the imaging result of "I" with polarization angles of 0° and 90° under 532 nm illumination. (c, d) is the imaging result of "I" with polarization angles of 0° and 90° under 976 nm illumination.

Table 1 | Comparison of performance between 1T'-$MoTe_2$/2H-$MoTe_2$ devices and other $MoTe_2$ heterojunction photodetectors.

Structure	V_{ds} (V)	Light (nm)	R ($A \cdot W^{-1}$)	EQE (%)	D^* (Jones)	τ_r/τ_d (ms)	Polarization sensitivity	Ref.
1T' -$MoTe_2$/2H -$MoTe_2$	1	1310	3.06	289	10^9	10.56/6.26	20.1	This work
GeSe/$MoTe_2$	0	808	0.052	-	10^{11}	80/26	5.4	ref.[33]
$MoTe_2$/WTe_2	0	635	0.6	-	10^{13}	590/1000	3.5	ref.[34]
Bi_2O_2Se/$MoTe_2$	0	1310	0.19	-	10^9	-	-	ref.[35]
$MoTe_2$/InSe	0	405	0.4	-	10^{12}	0.099/0.117	-	ref.[36]
$MoTe_2$/1T'-$MoTe_2$-$SnSe_2$	0	1310	0.0642	-	10^{11}	27/30	1.55	ref.[32]
$MoTe_2$/1T'-$MoTe_2$-$MoSe_2$	1	1310	0.76	71	10^9	13/10	55	ref.[37]

obtained at polarization angles using light sources with wavelengths ranging from 532 nm to 976 nm. It is worth noting that the heterostructure device accurately captures the "I" pattern at all excitation wavelengths, with clear and distinct boundaries between the pattern and the background, demonstrating the broadband polarization imaging capability of the 1T'-$MoTe_2$/2H-$MoTe_2$ device. It should be emphasized that the effective imaging window of heterostructure devices (532–976 nm) significantly exceeds human vision, bringing interesting prospects for future visual systems.

Table 1 compares the characteristics of this heterojunction device with other previously reported vdW heterojunction photodetectors based on $MoTe_2$ material. The 1T'-$MoTe_2$/2H-$MoTe_2$ heterojunction device exhibits excellent, competitive, and comprehensive self powered photodetection capabilities, as well as outstanding detection performance in polarized light detection. It has great potential for application in future polarized imaging near-infrared detectors.

4 Conclusions

In summary, we have developed a near-infrared polarization sensitive photodetector based on 1T'-$MoTe_2$/2H-$MoTe_2$ vdW heterojunction for multi band detection. The response band is in the wide spectral range of 532–2200 nm, and it has high light detection performance. The device has a high responsivity of 3.06 $A \cdot W^{-1}$ at 1310 nm, a high specific detectivity of 3.2×10^9 Jones, a high EQE of 289%, and fast rise and fall response times of 10.56 ms/6.26 ms. And further detection was conducted on the polarization sensitivity of the heterojunction in a wide spectral range (650–1310 nm), with a polarization sensitivity of 2.18 at 650 nm and 20.1 at 1310 nm. In addition, the device also demonstrates ultra wideband and polarized light imaging capabilities, making it competitive among the most advanced 2D material based devices and commercial products. This study developed a narrow bandgap vdW heterojunction consisting of an in-plane anisotropic 1T'-$MoTe_2$ layer and an isotropic 2H-$MoTe_2$ layer. This structure provides a new strategy for achieving wide spectrum, fast response, and high polarization sensitivity near-infrared imaging in optoelectronic devices, and provides a reliable basis for developing next-generation two-dimensional imaging electronic and optoelectronic devices.

References

1. Pan J, Wu YM, Zhang XJ et al. Anisotropic charge trapping in phototransistors unlocks ultrasensitive polarimetry for bionic navigation. *Nat Commun* **13**, 6629 (2022).
2. Li SN, Zhang JL, Zhu LY et al. Reconfigurable and broadband polarimetric photodetector. *Adv Funct Mater* **33**, 2210268 (2023).
3. Zhou ZQ, Shen T, Wang P et al. Low symmetric sub-wavelength array enhanced lensless polarization-sensitivity photodetector of germanium selenium. *Sci Bull* **68**, 173–179 (2023).
4. Sun D, Feng B, Yang B et al. Design and fabrication of an InGaAs focal plane array integrated with linear-array polarization grating. *Opt Lett* **45**, 1559–1562 (2020).
5. Kumar P, Pfeffer M, Berthold C et al. PbSe mid-IR photoconductive thin films (part-II): structural analysis of the functional layer. *J Alloys Compd* **735**, 1654–1661 (2018).
6. Saran R, Curry RJ. Lead sulphide nanocrystal photodetector technologies. *Nat Photonics* **10**, 81–92 (2016).
7. Fuls EN. Optical frequency mixing in photoconductive InSb. *Appl Phys Lett* **4**, 7–8 (1964).
8. Hu S, Bao P, Cao YH et al. Giant lateral photovoltaic effect in Ag/porous silicon/Si structure for high-performance near-infrared detection. *Nano Energy* **120**, 109167 (2024).
9. Michel J, Liu JF, Kimerling LC. High-performance Ge-on-Si photodetectors. *Nat Photonics* **4**, 527–534 (2010).
10. Lei W, Antoszewski J, Faraone L. Progress, challenges, and opportunities for HgCdTe infrared materials and detectors. *Appl Phys Rev* **2**, 041303 (2015).
11. Ren DK, Meng X, Rong ZX et al. Uncooled photodetector at short-wavelength infrared using InAs nanowire photoabsorbers on InP with *p-n* heterojunctions. *Nano Lett* **18**, 7901–7908 (2018).
12. Jia BW, Tan KH, Loke WK et al. Monolithic integration of InSb photodetector on silicon for mid-infrared silicon photonics. *ACS Photonics* **5**, 1512–1520 (2018).
13. Erhard N, Zenger S, Morkötter S et al. Ultrafast photodetection in the quantum wells of single AlGaAs/GaAs-based nanowires. *Nano Lett* **15**, 6869–6874 (2015).
14. Zhang FL, Zhang XT, Li ZY et al. A new strategy for selective area growth of highly uniform InGaAs/InP multiple quantum well nanowire arrays for optoelectronic device applications. *Adv Funct Mater* **32**, 2103057 (2022).
15. Long MS, Wang P, Fang HH et al. Progress, challenges, and opportunities for 2D material based photodetectors. *Adv Funct Mater* **29**, 1803807 (2019).
16. Jiang MH, Zheng T, Zhang JL et al. Gate-modulated polarity transition and polarization-sensitive photodetection enabled by sand-

wiching anisotropic GeSe in vdW heterojunction. *Adv Opt Mater* **12**, 2303217 (2024).
17. Yan Y, Xiong WQ, Li SS et al. Direct wide bandgap 2D $GeSe_2$ monolayer toward anisotropic UV photodetection. *Adv Opt Mater* **7**, 1900622 (2019).
18. Liu FC, Zheng SJ, He XX et al. Highly sensitive detection of polarized light using anisotropic 2D ReS_2. *Adv Funct Mater* **26**, 1169–1177 (2016).
19. Li KL, Du CH, Gao HL et al. Ultra-fast and linear polarization-sensitive photodetectors based on $ReSe_2/MoS_2$ van der Waals heterostructures. *J Materiomics* **8**, 1158–1164 (2022).
20. Wang J, Jiang CZ, Li WQ et al. Anisotropic low-dimensional materials for polarization-sensitive photodetectors: from materials to devices. *Adv Opt Mater* **10**, 2102436 (2022).
21. Zhao SW, Wu JC, Jin K et al. Highly polarized and fast photoresponse of black phosphorus-InSe vertical p-n heterojunctions. *Adv Funct Mater* **28**, 1802011 (2018).
22. Yuan HT, Liu XG, Afshinmanesh F et al. Polarization-sensitive broadband photodetector using a black phosphorus vertical p-n junction. *Nat Nanotechnol* **10**, 707–713 (2015).
23. Wang XT, Zhong F, Kang J et al. Polarizer-free polarimetric image sensor through anisotropic two-dimensional GeSe. *Sci China Mater* **64**, 1230–1237 (2021).
24. Kim DH, Lee R, Kim S et al. Two-dimensional phase-engineered 1T′- and 2H-$MoTe_2$-based near-infrared photodetectors with ultra-fast response. *J Alloys Compd* **789**, 960–965 (2019).
25. Ahmed F, Rodríguez-Fernández C, Fernandez HA et al. Deterministic polymorphic engineering of $MoTe_2$ for photonic and optoelectronic applications. *Adv Funct Mater* **33**, 2302051 (2023).
26. Wu ZQ, Chen MF, Liu XY et al. Sandwiched $WS_2/MoTe_2/WS_2$ heterostructure with a completely depleted interlayer for a photodetector with outstanding detectivity. *ACS Appl Mater Interfaces* **16**, 36609–36619 (2024).
27. Wang HY, Li Y, Gao P et al. Polarization- and gate-tunable optoelectronic reverse in 2D semimetal/semiconductor photovoltaic heterostructure. *Adv Mater* **36**, 2309371 (2024).
28. Chen WJ, Liang RR, Zhang SQ et al. Ultrahigh sensitive near-infrared photodetectors based on $MoTe_2$/germanium heterostructure. *Nano Res* **13**, 127–132 (2020).
29. Wu D, Guo CG, Zeng LH et al. Phase-controlled van der Waals growth of wafer-scale 2D $MoTe_2$ layers for integrated high-sensitivity broadband infrared photodetection. *Light Sci Appl* **12**, 5 (2023).
30. Zhao DY, Chen Y, Jiang W et al. Gate-tunable photodiodes based on mixed-dimensional $Te/MoTe_2$ Van der Waals heterojunctions. *Adv Electron Mater* **7**, 2001066 (2021).
31. Zhao Y, Cho J, Choi M et al. Light-tunable polarity and erasable physisorption-induced memory effect in vertically stacked $InSe/SnS_2$ self-powered photodetector. *ACS Nano* **16**, 17347–17355 (2022).
32. Sun YM, Xiong JX, Wu XM et al. Highly sensitive infrared polarized photodetector enabled by out-of-plane PSN architecture composing of p-$MoTe_2$, semimetal-$MoTe_2$ and n-$SnSe_2$. *Nano Res* **15**, 5384–5391 (2022).
33. Zhang N, Wu LW, Gao W et al. Near-infrared, self-powered and polarization-sensitive photodetector based on GeSe-$MoTe_2$ p-n heterojunction. *Adv Mater Interfaces* **9**, 2200150 (2022).
34. Wang SJ, Qi LG, Xia ZH et al. Polarization-sensitive detector based on $MoTe_2/WTe_2$ heterojunction for broadband optoelectronic imaging. *J Phys Chem Lett* **14**, 10509–10516 (2023).
35. Dan ZY, Yang BX, Song QQ et al. Type-II $Bi_2O_2Se/MoTe_2$ van der Waals heterostructure photodetectors with high gate-modulation photovoltaic performance. *ACS Appl Mater Interfaces* **15**, 18101–18113 (2023).
36. He SX, Feng P, Du Y et al. High performance self-powered and vis-infrared broadband photodetectors based on $MoTe_2$/InSe Van der Waals heterostructure. *Adv Opt Mater* **12**, 2302399 (2024).
37. Pan YT, Zhu LQ, Lu LD et al. Polarized photodetectors based on 2D 2H-$MoTe_2$/1T'-$MoTe_2$/$MoSe_2$ Van Der Waals heterojunction. *Adv Funct Mater* **34**, 2407931 (2024).

Acknowledgements

We are grateful for financial supports from the National Natural Science Foundation of China (62205029) and the Young Elite Scientists Sponsorship Program by CAST (No.YESS20220267).

Author contributions

All authors commented on the manuscript. Yuting Pan proposed the initial idea and supervised the project. Lianqing Zhu, Lidan Lu, and Jianzhen Ou supervised the project, while other authors guided the work, with equal contributions.

Competing interests

The authors declare no competing financial interests.

Supplementary information

Supplementary information for this paper is available at
https://doi.org/10.29026/oea.2026.250260

Published by Editorial Office of *Opto-Electronic Advance*, Institute of Optics and Electronics, Chinese Academy of Sciences.

Opto-Electronic Journals Group
www.oejournal.org
Scan for Article PDF